

# Probabilistic Spatial Transformers for Bayesian Data Augmentation

Pola Schwöbel<sup>1</sup> Frederik Warburg<sup>1</sup> Martin Jørgensen<sup>1</sup> Kristoffer H. Madsen<sup>2,1</sup> Søren Hauberg<sup>1</sup>

## Abstract

High-capacity models require vast amounts of data, and data augmentation is a common remedy when this resource is limited. Standard augmentation techniques apply small hand-tuned transformations to existing data, which is a brittle process that realistically only allows for simple transformations. We propose a Bayesian interpretation of data augmentation where the transformations are modelled as latent variables to be marginalized, and show how these can be inferred variationally in an end-to-end fashion. This allows for significantly more complex transformations than manual tuning, and the marginalization implies a form of test-time data augmentation. The resulting model can be interpreted as a probabilistic extension of spatial transformer networks. Experimentally, we demonstrate improvements in accuracy and uncertainty quantification in image and time-series classification tasks.

## 1. Introduction

Training deep neural networks and other large models is crucially dependent on the availability of large annotated data sets (Deng et al., 2009; Lin et al., 2014). Unfortunately, not all domains of science are as data-rich as needed, and this effectively limits the practical application of algorithms. In the medical domain, for instance, data is often expensive to both acquire and annotate, and the amount of data is naturally limited by the number of affected patients.

*Data augmentation (DA)* is a simple, yet efficient, engineering trick to overcome this limitation. The idea is to artificially generate new data through small transformations of existing data. Its application for machine learning prob-

<sup>1</sup>Section for Cognitive Systems, Department of Applied Mathematics and Computer Science, Technical University of Denmark, Copenhagen, Denmark <sup>2</sup>Danish Research Centre for Magnetic Resonance, Centre for Functional and Diagnostic Imaging and Research, Copenhagen University Hospital Hvidovre, Hvidovre, Denmark. Correspondence to: Pola Schwöbel <posc@dtu.dk>.

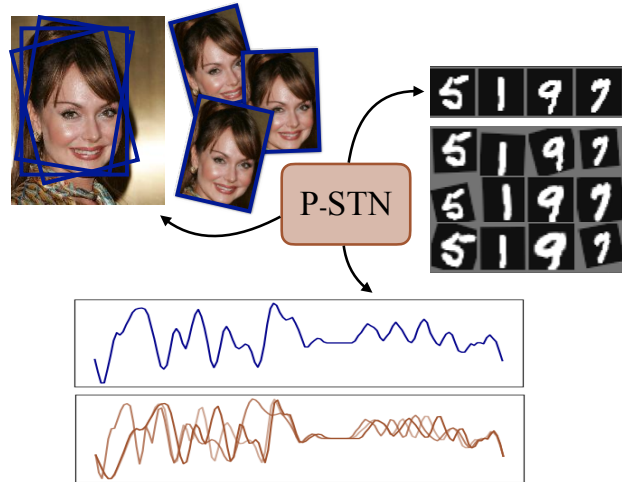


Figure 1. The Probabilistic Spatial Transformer provides a unified framework for learning Bayesian data augmentation for different data modalities.

lems dates back to the nineties (LeCun et al., 1995), and even further in the statistics community (Tanner & Wong, 1987). Training on the augmented data often significantly improves model fit and the DA is considered part of good practice (Krizhevsky et al., 2012b).

The underlying assumption is that the target prediction of an observation is invariant to small transformations of the input, e.g. that a new image can be generated by slightly rotating an existing one. A high-quality DA scheme, thus, relies on manual specification of a suitable collection of invariances; a process not unlike classic *feature engineering*, where the goal is to derive features with requested invariances. As such, developing a DA scheme is a brittle process that may require significant hand-tuning with all the pitfalls this entails. For image data, there exists a reasonably well-understood set of default transformations (rotations, scalings, etc.), but for most data modalities no such defaults are available. These observations all points toward *learning DA* rather than relying on manual specification.

If we assume an additive loss function  $\frac{1}{N} \sum_{n=1}^N \mathcal{L}(x_n)$ , then DA can be written as  $\frac{1}{NM} \sum_{n=1}^N \sum_{m=1}^M \mathcal{L}(T_m(x_n))$ , where  $T_m$  is a random transformation and each observation  $x_n$  is augmented to form  $M$  new ones. Taking the limit  $M \rightarrow \infty$

we see that this augmented loss function can, from a probabilistic perspective, be seen as a marginalization of a random latent transformation. It is exactly this view point we shall take, from which we will derive an end-to-end learnable DA model that is applicable to any spatio-temporal data modality. Practically speaking, the resulting model can be seen as a probabilistic extension of the *spatial transformer network* (Jaderberg et al., 2015), where we apply a variational approximation.

## 2. Related Work

**Data augmentation (DA)** is commonly applied as a means to increase the amount of available data (LeCun et al., 1995). Formally, given a data set  $\mathcal{D} = \{x_n, y_n\}_{n=1}^N$  consisting of  $N$  input-output pairs, DA creates a new data set

$$\mathcal{D}_{\text{aug}} = \left\{ \left\{ T_{\theta_m}(x_n), y_n \right\}_{m=1}^M \right\}_{n=1}^N, \quad \theta_m \sim p(\theta), \quad (1)$$

where  $T_\theta : \mathbb{R}^E \rightarrow \mathbb{R}^E$  is a transformation (parametrized by  $\theta$ ) that modifies an observation to create a new one. DA is particularly common for image data, where the transformation family is most commonly chosen to be affine transformations such as rotations, scalings, etc. (Goodfellow et al., 2009; Baird, 1992; Simard et al., 2003; Krizhevsky et al., 2012a; Loosli et al., 2007).

DA constitutes a strong prior when it is known that the target  $y_n$  is invariant to certain transformations of the observation  $x_n$ . Gathering such a prior is, however, non-trivial for most data modalities (with image data being the key exception), and a wrong choice can decrease model performance significantly (Engstrom et al., 2017). For instance, in speech recognition, *Vocal Tract Normalization (VTLN)* (Jaitly & Hinton, 2013) transforms utterances of one speaker to another through spectral warps, and in galaxy redshift prediction (Hoyle et al., 2015) augmentation requires pre-developed redshift models. The general trend is that, beyond image data, DA is often difficult to realize.

**Learned data augmentation** provides a more principled approach to artificially extending datasets. Hauberg et al. (2016) estimate an augmentation scheme from the training data via pre-aligning images in an unsupervised manner. The approach allows for significantly more complex transformations than the usual affine family, but the approach lacks principle and the unsupervised nature renders the approach suboptimal. Tran et al. (2017) present a Bayesian treatment of data augmentation where, similar to our approach, the augmentations are treated as a latent variable. The algorithm, however, does not perform data augmentation in the strict sense of “*transformed images to be produced from the original images with very little computation*” (Krizhevsky et al., 2012b). Instead, the new images are generated from scratch via a GAN (Goodfellow et al., 2014). While conceptually interesting, the approach is limited as

learning a full-blown generative model is sufficiently more complicated than solving the final supervised task.

Van der Wilk et al. (2018) learn DA for a Gaussian process (GP) via the marginal likelihood, a quantity that is generally hard to compute but can be estimated for GPs with simple kernels. Computing marginal likelihoods for neural networks is a part of the active area of research within Bayesian deep learning (Blundell et al., 2015), but currently remains unfeasible (Blei et al., 2017). Our model demonstrates that it suffices to only marginalize the transformation parameters, and that a variational lower bound is a viable substitute for the marginal likelihood.

**Spatial transformer networks (STNs)** apply a spatial transformation to the input data as part of an end-to-end trained neural network (Jaderberg et al., 2015). The transformation parameters are estimated from each input separately through a neural network. Most commonly, STNs implement simple affine transformations, such that the network can learn to crop out the relevant parts of an image before solving the task at hand. STNs have shown themselves to be useful for both generative and discriminative tasks, using both affine and more complex transformations, and have seen uses in different data modalities (Jaderberg et al., 2015; Detlefsen & Hauberg, 2019; Detlefsen et al., 2018; Shapira Weber et al., 2019; Sønderby et al., 2015; Lin & Lucey, 2016; Kanazawa et al., 2016). Our work can be seen as a probabilistic extension of this idea, replacing the usual maximum likelihood estimation with marginalization.

**Uncertainty quantification** is difficult in highly over-parametrized deep neural networks. Guo et al. (2017) are concerned with neural networks’ calibration properties and the overconfidence issue of such models. They identify temperature scaling, a smoothening method for the softmax activation function which is prominently applied for knowledge distillation by Hinton et al. (2015), as a way to achieve calibration. *Test-time data augmentation* offers another possible solution for overconfident models. Wang et al. (2018) suggest to marginalize image transformations by sampling augmented images from a prior in order to increase entropy of the predictive distribution. In contrast, our proposed model samples from a posterior distribution.

## 3. Probabilistic Spatial Transformer

In order to introduce the proposed DA model, we first establish notation. We assume observed data of the form  $\mathcal{D} = \{y_i, I_{\text{obs}_i}\}_{i=1}^N$ , where  $y$  is the target variable (e.g. class label), and  $I_{\text{obs}}$  are observations of the covariates. For presentation purposes, we will consider the latter to be images, but the approach applies to any spatio-temporal data.

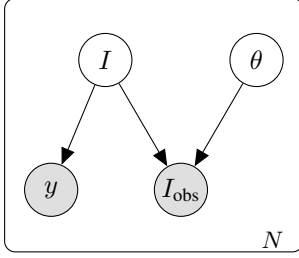


Figure 2. A graphical representation of the model structure. Grey nodes are observables and white are latents.

### 3.1. The Model

The *Probabilistic Spatial Transformer (P-STN)* combines a generative and a discriminative model. Sampling from the generative model corresponds data augmentation, and both models are trained jointly. The key assumption is that an observed image  $I_{\text{obs}}$  is generated by transforming a true, unobserved image  $I$  with an unknown image transformation parametrized by  $\theta$ . The generative model is thus governed by two latent variables: the underlying pre-image  $I$  and the transformation  $\theta$  whose distribution we are estimating to recover the true image  $I$  and eventually classify it.

Marginalizing those latent variables, our objective will be to maximize

$$\log p(I_{\text{obs}}, y) = \log \int p(I_{\text{obs}}, y, I, \theta) dI d\theta. \quad (2)$$

We let the joint distribution factorize as (see Fig. 2)

$$p(I_{\text{obs}}, y, I, \theta) = p(y|I)p(I_{\text{obs}}|I, \theta)p(\theta)p(I), \quad (3)$$

where we assume a non-informative prior  $p(I)$  over the true images as an informative one is generally not tractable to obtain. Out of simplicity we assume a Gaussian prior over the transformation parameters

$$p(\theta) = \mathcal{N}(\theta|0, \sigma_p^2 \text{Id}_D), \quad (4)$$

where  $\text{Id}_D$  denotes the identity matrix of size  $D = \dim(\theta)$ . Finally, we assume that the observed image is generated by transforming the true image and adding Gaussian noise,

$$p(I_{\text{obs}}|I, \theta) = \mathcal{N}(I_{\text{obs}}|T_\theta^{-1}(I), \sigma_{\text{noise}}^2 \text{Id}_d), \quad (5)$$

where  $d$  is the dimensionality of the images (i.e. number of pixels). Here we assume that the transformations  $T$  are smooth and invertible (see Sec. 4.1 for details). Finally, we assume that, conditional on  $I$ , we have marginal independence, i.e.  $p(y|I) = \prod_{i=1}^N p(y_i|I_i)$ .

### 3.2. Variational Approximation

The integral equation (2) for the marginal likelihood is intractable (and so is the posterior  $p(I, \theta|I_{\text{obs}}, y)$ ). Following

Kingma & Welling (2019), we use variational inference to derive a lower bound that we can optimize. We choose the variational approximation of the posterior  $p(I, \theta|I_{\text{obs}}, y)$  as

$$q(I, \theta|I_{\text{obs}}, y) := q(I|\theta, I_{\text{obs}})q(\theta|I_{\text{obs}}), \quad \text{where} \quad (6)$$

$$q(I|\theta, I_{\text{obs}}) := \mathcal{N}(I|T_\theta(I_{\text{obs}}), \sigma_{\text{noise}}^2 \text{Id}_d), \quad (7)$$

$$q(\theta|I_{\text{obs}}) := \mathcal{N}(\mu(I_{\text{obs}}), \Sigma(I_{\text{obs}})). \quad (8)$$

Here,  $\mu(I_{\text{obs}})$ ,  $\Sigma(I_{\text{obs}})$  are functions parametrized by neural networks, i.e.  $\mu(I_{\text{obs}}) := \mu_\Phi(I_{\text{obs}})$ ,  $\Sigma(I_{\text{obs}}) := \Sigma_\Phi(I_{\text{obs}})$  for model parameters  $\Phi$ .

We can then write our objective as

$$\log p(I_{\text{obs}}, y) = \mathbb{E}_{q(I, \theta|I_{\text{obs}}, y)}[\log p(I_{\text{obs}}, y)] \quad (9)$$

$$= \mathbb{E}_{q(I, \theta|I_{\text{obs}}, y)} \left[ \log \left[ \frac{p(I_{\text{obs}}, y, I, \theta)}{p(I, \theta|I_{\text{obs}}, y)} \right] \right] \quad (10)$$

$$= \mathbb{E}_{q(I, \theta|I_{\text{obs}}, y)} \left[ \log \left[ \frac{p(I_{\text{obs}}, y, I, \theta)q(I, \theta|I_{\text{obs}}, y)}{q(I, \theta|I_{\text{obs}}, y)p(I, \theta|I_{\text{obs}}, y)} \right] \right] \quad (11)$$

$$= \mathbb{E}_{q(I, \theta|I_{\text{obs}}, y)} \left[ \log \left[ \frac{p(I_{\text{obs}}, y, I, \theta)}{q(I, \theta|I_{\text{obs}}, y)} \right] \right] \quad (12)$$

$$\underbrace{\mathbb{E}_{q(I, \theta|I_{\text{obs}}, y)} \left[ \log \left[ \frac{p(I_{\text{obs}}, y, I, \theta)}{q(I, \theta|I_{\text{obs}}, y)} \right] \right]}_{=: \mathcal{L}_{p, q}(I_{\text{obs}}, y)} + \underbrace{\mathbb{E}_{q(I, \theta|I_{\text{obs}}, y)} \left[ \log \left[ \frac{q(I, \theta|I_{\text{obs}}, y)}{p(I, \theta|I_{\text{obs}}, y)} \right] \right]}_{= KL(q(I, \theta|I_{\text{obs}}, y) || p(I, \theta|I_{\text{obs}}, y))} \quad (13)$$

Since  $KL(\cdot||\cdot) \geq 0$  we see that  $\mathcal{L}_{p, q}$  is a lower bound (the *ELBO*) for  $\log p(I_{\text{obs}}, y)$ . Using the factorization from Eq. 3, the ELBO decomposes into

$$\mathcal{L}_{p, q}(I_{\text{obs}}, y) = \mathbb{E}_{q(I, \theta|I_{\text{obs}}, y)}[\log p(I_{\text{obs}}, y, I, \theta)] \quad (14)$$

$$- \mathbb{E}_{q(I, \theta|I_{\text{obs}}, y)}[\log q(I, \theta|I_{\text{obs}}, y)]$$

$$= \mathbb{E}_{q(I, \theta|I_{\text{obs}}, y)}[\log p(y|I) + \log p(I_{\text{obs}}|I, \theta)] \quad (15)$$

$$- \mathbb{E}_{q(I, \theta|I_{\text{obs}}, y)}[\log q(I, \theta|I_{\text{obs}}, y) - \log p(I, \theta)]$$

$$= \underbrace{\mathbb{E}_{q(I, \theta|I_{\text{obs}}, y)}[\log p(y|I)]}_{\text{(classification loss)}} \quad (16)$$

$$+ \underbrace{\mathbb{E}_{q(I, \theta|I_{\text{obs}}, y)}[\log p(I_{\text{obs}}|I, \theta)]}_{\text{(reconstruction loss)}} \quad (17)$$

$$- \underbrace{KL(q(I, \theta|I_{\text{obs}}, y) || p(I, \theta))}_{\text{(regularization loss)}}. \quad (18)$$

Thus, our loss function,  $\mathcal{L}_{p, q}(I_{\text{obs}}, y)$ , consists of three terms: classification loss, reconstruction loss from the generative model, and a regularization term controlling the distance of the approximate posterior to the prior. Per usual variational inference, this can then be optimized with respect to  $\Phi$  and the classifier parameters.

### 3.3. Inference

The expectation in the **classification loss** is computed via Monte Carlo and amounts to sampling and classifying augmented images,

$$\mathbb{E}_{q(I, \theta | I_{\text{obs}}, y)}[\log p(y|I)] \approx \frac{1}{S} \sum_{s=1}^S \log p(y|I_s), \quad (19)$$

$$\text{with } \theta_s \sim \mathcal{N}(\mu(I_{\text{obs}}), \Sigma(I_{\text{obs}})), \quad (20)$$

$$\text{and } I_s | \theta_s \sim \mathcal{N}(T_{\theta_s}(I_{\text{obs}}), \sigma_{\text{noise}}^2 \text{Id}_d). \quad (21)$$

As suggested by Kingma & Welling (2014), we choose the number of samples  $S = 1$  during training unless stated otherwise. At test time, we increase this to  $S = 10$ .

If we assume  $T_{\theta}^{-1}(I) = I_{\text{obs}}$ , i.e. no noise or interpolation artifacts, then the **reconstruction loss**  $\mathcal{N}(I_{\text{obs}} | I_{\text{obs}}, \sigma_{\text{noise}}^2 \text{Id}_d)$  constant. In the low noise setting it is still roughly constant (and small), due to the norm of  $T$  and  $T_{\theta}^{-1}$  being bounded. See supplementary material for a more detailed discussion. The practical implication is that the reconstruction loss can be ignored during optimization.

Since the prior over the true images  $p(I)$  is non-informative,  $KL(q(I|\theta, I_{\text{obs}}) || p(I))$  is constant independent of  $\theta$ . The **regularization loss** thus reduces to

$$KL(q(I, \theta | I_{\text{obs}}, y) || p(I, \theta)) = KL(q(\theta | I_{\text{obs}}) || p(\theta)) + \text{const}, \quad (22)$$

where the  $KL$ -divergence between the two normal distributions  $KL(q(\theta | I_{\text{obs}}) || p(\theta))$  can be computed in closed form.

Combining terms, the final ELBO becomes

$$\mathcal{L}_{p,q}(I_{\text{obs}}, y) \approx \frac{1}{S} \sum_{s=1}^S \log p(y|I_s) + KL(q(\theta | I_{\text{obs}}) || p(\theta)) + \text{const}, \quad (23)$$

which is readily optimized using any gradient-based method.

## 4. Transformation and Implementation Details

### 4.1. Parametrizing Image Transformations

The P-STN model estimates  $\theta$ , the parameters of transformations  $T_{\theta}$  used for data augmentation. So far, the relationship between such parameters and image transformation has been abstract, but we now describe two such families.

#### 4.1.1. AFFINE TRANSFORMATIONS

In order to learn our end-to-end data augmentation scheme, we need to parametrize our image transformations in a differentiable manner. A simple class of transformations that

can be differentially parametrized are affine transformations. We limit ourselves to the subset of affine transformations containing rotation, isotropic scaling and translation in  $x$  and  $y$ . In two dimensions (and the corresponding three-dimensional homogeneous coordinates), we thus learn  $\theta = (\alpha, s, t_x, t_y)$  which parametrizes the affine matrix

$$A_{\theta} = \begin{bmatrix} s \cdot \cos \alpha & -s \cdot \sin \alpha & t_x \\ s \cdot \sin \alpha & s \cdot \cos \alpha & t_y \\ 0 & 0 & 1 \end{bmatrix} \in \mathbb{R}^{3 \times 3}, \quad s > 0. \quad (24)$$

Since  $\det(A_{\theta}) = s^2$ , the constraint  $s > 0$  ensures invertibility and can be implemented as seen in Detlefsen et al. (2018). In practice, our model estimates such well-behaved, non-collapsing transformations without implementing the constraint explicitly.  $T_{\theta}(I_{\text{obs}})$  is applied by transforming the a grid of the target image size by  $A_{\theta}$  and interpolating the source image at the resulting coordinates (see Jaderberg et al. (2015) for details).

#### 4.1.2. DIFFEOMORPHIC TRANSFORMATIONS

Low-dimensional affine transformations are limited in their expressiveness. Freifeld et al. (2017) construct more general diffeomorphisms (i.e. transformations that are differentiable, invertible and possess a differentiable inverse) from continuous piecewise-affine velocity fields as follows. The transformation domain  $\Omega$  (i.e.  $\Omega \subset \mathbb{R}^2$  for 2d images) is divided into subsets and an affine matrix is defined on each cell  $c$  of such a tessellation. Each affine matrix  $A_{\theta_c}$  induces a vector field mapping each point  $x \in c$  to a new position  $v^{\theta_c} : x \mapsto A_{\theta_c} x$ . These velocity fields are then integrated to form a trajectory for each image point  $x$

$$\phi^{\theta}(x; 1) = x + \int_0^1 v^{\theta}(\phi(x; \tau)) d\tau.$$

Given boundary and invertibility constraints (Freifeld et al., 2017), such a collection of affine matrices  $\{A_{\theta_c}\}_{c \subset \Omega}$  defines a diffeomorphic transformation  $T^{\theta} : x \mapsto \phi^{\theta}(x, 1)$ . The libcpab library (Detlefsen, 2018) provides an efficient implementation for this approach, specifically optimized for use in a deep learning context where fast gradient evaluations are crucial. The author successfully employs CPAB-transformations within a Spatial Transformer Network (Detlefsen et al., 2018).

A transformation is then identified with a vector  $\theta \in \mathbb{R}^D$ , where  $D = 4$  in the affine case. In the diffeomorphic case  $D$  depends on the resolution of the tessellation. The distributions over the transformations  $q(\theta | I_{\text{obs}})$  that we aim to model thus become simple multivariate Gaussians where we choose diagonal covariances

$$q(\theta | I_{\text{obs}}) = \mathcal{N}(\mu(I_{\text{obs}}), \Sigma(I_{\text{obs}})) \text{ with} \quad (25)$$

$$\Sigma(I_{\text{obs}}) = \text{diag}(\sigma_1^2(I_{\text{obs}}), \dots, \sigma_D^2(I_{\text{obs}})). \quad (26)$$

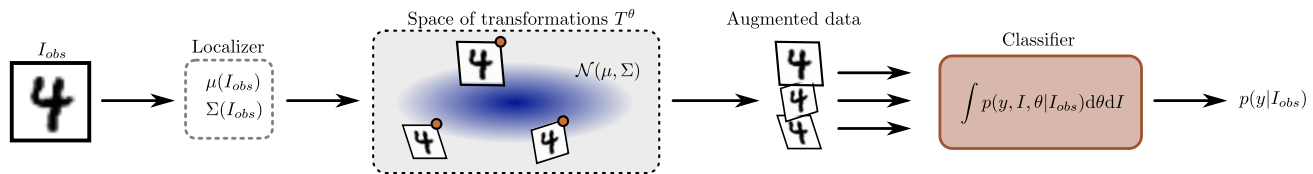


Figure 3. The P-STN pipeline. From the observed image  $I_{obs}$ , a distribution of transformations are estimated. Samples from this distribution are applied to the observed image to produce augmented samples, which are fed to a classifier that average across samples.

## 4.2. Sampling transformation parameters

We draw samples  $\theta_s \sim \mathcal{N}(\mu(I_{obs}), \Sigma(I_{obs}))$  and optimize the parameters of the neural networks  $\mu(\cdot)$  and  $\Sigma(\cdot)$ . For our end-to-end learning approach, we depend on a differentiable generator for  $\theta$  and therefore rewrite  $q(\theta | I_{obs})$  using the usual “reparametrization trick” (Kingma & Welling, 2014). That is, we draw  $\epsilon_s \sim \mathcal{N}(0_D, \text{Id}_D)$  and combine

$$\theta_s = \mu(I_{obs}) + \text{diag}(\sigma_1(I_{obs}), \dots, \sigma_D(I_{obs})) \odot \epsilon_s,$$

thereby obtaining deterministic functions  $\mu(I_{obs}), \Sigma(I_{obs})$  whose parameters can be optimized via gradient descent.

## 4.3. Traditional Data Augmentation

We will benchmark our learned DA against traditional, ad-hoc data augmentation. For increased comparability and control, we implement a custom ad-hoc data augmentation scheme which samples transformations similarly to the P-STN. We draw transformations

$$\theta \sim \mathcal{N}(0, \Sigma_{DA}) = \mathcal{N}(0, \sigma_{DA}^2 \text{Id}_D).$$

In contrast to the P-STN model,  $\sigma_{DA}$  is chosen a priori rather than estimated from the data and the sampling is performed before feeding the data into the model.

## 4.4. Deep Learning Architecture

Our model consists of two parts, the classifier which seeks to compute  $p(y | I_s)$  and the Probabilistic Spatial Transformer module which estimates the transformation distributions  $q(\theta | I_{obs}) = \mathcal{N}(\theta | \mu(I_{obs}), \Sigma(I_{obs}))$ , samples a transformation  $T_\theta$  and then applies it by transforming a coordinate grid and interpolating the image accordingly. The architecture is visualized in Fig. 3. A modular implementation allows for a flexible choice of network architecture for the classifier and the mean and variance networks. In our experiments, we chose all of them to be simple convolutional neural networks. Our model is implemented in PyTorch and experiments are run on a 12 GB Nvidia Titan X GPU.

## 5. Experiments

We now quantitatively and qualitatively evaluate the P-STN on several datasets with different data modalities. The model

is compared to strong baselines, however, we show improvements in all experiments. We especially wish to highlight the ease in which the P-STN can be calibrated by tuning the prior  $\sigma_p$ .

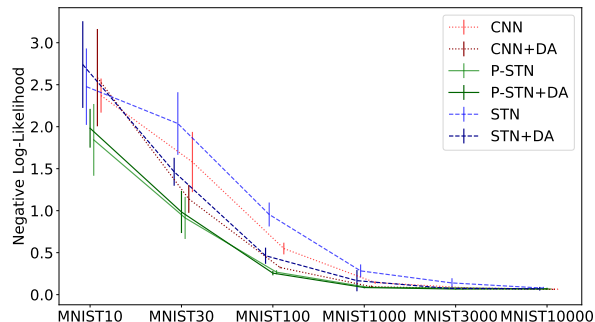
### 5.1. MNIST and subsets

We compare the performance of our Probabilistic Spatial Transformer Network (P-STN) model against a standard convolutional neural network (CNN) and a Spatial Transformer Network (STN). Since we are interested in evaluating our learned data augmentation scheme, we additionally run all models with conventional data augmentation (+DA) as described in Sec. 4.3 for a more fair comparison. To analyse the importance of data augmentation for different dataset sizes, we evaluate the models on subsets of the MNIST dataset with different sizes: MNIST10 consisting of 10 images (i.e. 1 per class), MNIST30, MNIST100, MNIST1000, MNIST3000 and MNIST10000. In the first part of the experiment, both STN and P-STN parametrize affine transformations, i.e. the learned  $\theta$  is interpreted as a matrix as described in Sec. 4.1.1. All models have roughly the same amount of parameters (28k/44k for the affine and diffeomorphic case, respectively). In practice, this means that we reduce the classifier size for the STN and P-STN models when we add the localizer parameters. Code will be made available via the supplements. We use the Adam optimizer with weight decay 0.01 and the default parameters of its PyTorch implementation. The images are color normalized. We repeat the experiment 5 times, each time with a different  $k$ -image subset of the MNIST dataset, and we report  $\pm$  one standard deviation in tables and error bars. From Table 1 and Fig. 4, we see that the P-STN outperforms both the STN and CNN across all dataset sizes, however most notably, we see a large increase in performance for smaller datasets. This is particularly obvious from the negative log-likelihood and supports our claim that data augmentation is especially useful when data is a limited resource.

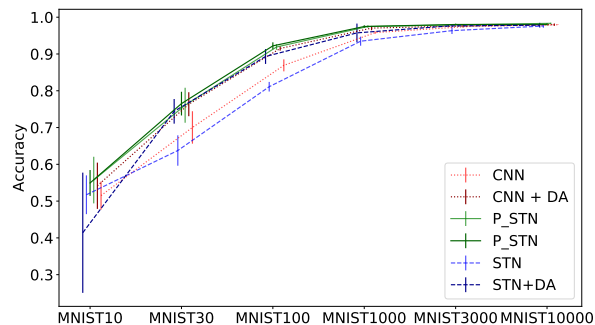
In this experiment, we also compare the affine and diffeomorphic transformations for both the STN and P-STN. Table 1 shows that using the diffeomorphic instead of the affine transformations increase performance further for both the STN and P-STN as it allows more flexible transformations. Besides improving upon the benchmark models on the

|                     | MNIST10                | MNIST30                | MNIST100               | MNIST1000              | MNIST3000              | MNIST10000             |
|---------------------|------------------------|------------------------|------------------------|------------------------|------------------------|------------------------|
| <i>CNN</i>          | 0.5151 ± 0.0381        | 0.7002 ± 0.0441        | 0.8690 ± 0.0163        | 0.9583 ± 0.0031        | 0.9746 ± 0.0016        | 0.9796 ± 0.0001        |
| <i>affine STN</i>   | 0.5172 ± 0.0527        | 0.6375 ± 0.0413        | 0.8110 ± 0.0131        | 0.9348 ± 0.0123        | 0.9634 ± 0.0092        | 0.9761 ± 0.0047        |
| <i>affine P-STN</i> | 0.5572 ± 0.0634        | 0.7606 ± 0.0476        | 0.9191 ± 0.0077        | <b>0.9747 ± 0.0035</b> | 0.9787 ± 0.0013        | <b>0.9829 ± 0.0025</b> |
| <i>diffeo STN</i>   | 0.5204 ± 0.0590        | 0.6945 ± 0.0315        | 0.8707 ± 0.0139        | 0.9578 ± 0.0048        | 0.9730 ± 0.0037        | 0.9791 ± 0.0022        |
| <i>diffeo P-STN</i> | <b>0.5728 ± 0.0858</b> | <b>0.7865 ± 0.0399</b> | <b>0.9344 ± 0.0013</b> | 0.9729 ± 0.0040        | <b>0.9795 ± 0.0015</b> | 0.9816 ± 0.0016        |

Table 1. The performance of a CNN, STN and P-STN on differently sized MNIST datasets. We experiment with both an affine and diffeomorphic transformation for both the STN and the P-STN. We see that the P-STN with the diffeomorphic transformation has the best cross-dataset performance.



(a) Negative log-likelihoods of the true labels for the different models as a function of dataset size.



(b) Accuracy as a function of dataset size.

Figure 4. Expected log-likelihood (a) and accuracy (b) for the P-STN, STN and CNN with traditional DA on MNIST subsets of different sizes. Here  $\sigma_p = \sigma_{DA} = 0.05$ .

MNIST dataset, our model is significantly better calibrated as will be discussed in the following.

*Model Uncertainty and Calibration:* Our learned data augmentation scheme can be canonically applied at test-time when we evaluate

$$\frac{1}{S} \sum_{s=1}^S p(y|I_s) \approx \int p(y|I)q(I|\theta, I_{\text{obs}})q(\theta|I_{\text{obs}}) dI d\theta \quad (27)$$

$$\approx \int p(y|I)p(I|\theta, I_{\text{obs}})p(\theta|I_{\text{obs}}) dI d\theta \quad (28)$$

$$= \int p(y, I, \theta|I_{\text{obs}}) dI d\theta = p(y|I_{\text{obs}}), \quad (29)$$

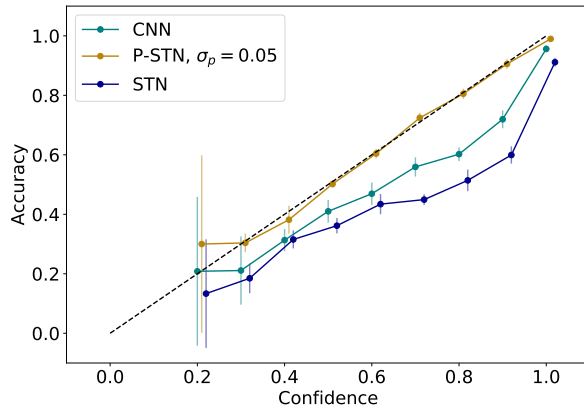


Figure 5. Calibration plot for the CNN, STN, P-STN model. CNN and STN are overconfident while the P-STN is well-calibrated. As above, we repeat the experiment 5 times, each time with a different 100-image subset of the MNIST dataset and report  $\pm$  one standard deviation in the error bars.

as derived in Sec. 3.3. From this we can compare our model’s uncertainty quantification to other models. Comparing the calibration plots for the CNN, STN and P-STN in Fig. 5, we see that both the CNN and STN are overconfident in their predictions, whereas the P-STN is well calibrated (close to the black dotted diagonal line). As expected, wider priors for the P-STN model correspond to more uncertainty in the predictions. The  $\sigma_p$  hyperparameter can thus be viewed as a simple, one parameter mechanism to regulate model uncertainty. For the affine MNIST100 experiment above, close to ideal calibration can be achieved with a value of  $\sigma_p = 0.05$  (see Fig. 6). In summary, the P-STN proves a superior model both quantitatively in negative log-likelihood and accuracy as well as qualitatively in uncertainty quantification.

## 5.2. MNIST $\times$ KMNIST

In this task, we utilize the P-STN as a differentiable attention mechanism to find discriminate objects. We construct a dataset consisting of two important objects to show that the P-STN can be used as an attention mechanism. The constructed dataset consists of two digits: one from MNIST

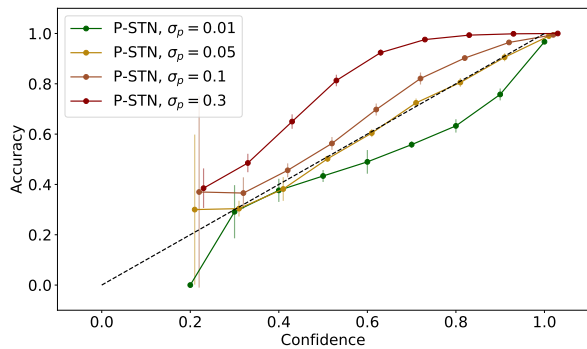


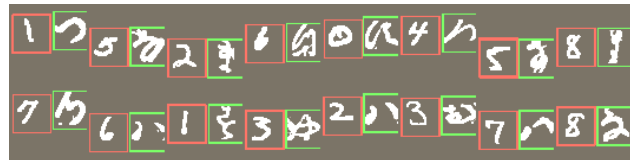
Figure 6. Calibration plots for the P-STN model at different priors on the MNIST100 experiment. The P-STN’s calibration can be conveniently tuned via the  $\sigma_p$  parameter, and an almost perfectly calibrated classifier (golden line) is achieved with  $\sigma_p = 0.05$ .

and one from KMNIST. The digits are placed at random positions in respectively the right and left side of the image and their labels are concatenated (See Fig. 7), such that we in total have 100 classes. We compare the performance of three models: *First*: a simple classifier composed of three convolutional layers with max pooling, relu, and dropout between each layer followed by two fully connected layers also with dropout and relu. *Second*: a STN where the localizer and the classifier has the same architecture as described above, but where the final fully connected layers of the localizer predicts two crops that are parameterized by  $x, y$  coordinates. We train two classifiers, one for each crop such that one specializes in Arabic digits and the other in Korean digits. We then pass the concatenated output of the classifiers through a fully connected layer to make a final prediction. This is a similar setup as presented by Jaderberg et al. (2015). *Third*: a P-STN that follows the same structure as the STN, but where the P-STN replaces the STN module. For the P-STN, we sample 2 times during training and 10 times for testing as we found this to increase the robustness of the training. The crops were initialized with tiling for both the P-STN and the STN. All models are trained with SGD with learning rate 0.1 for the classifier and 0.01 for the localizer. We use momentum 0.9 and weight decay of  $1^{-5}$ .

Figure 7 shows the predictions of the P-STN. The red and green bounding boxes show the parameterized crop predictions of the P-STN, which is the input for each of the classifiers. Note that, after training, the digits are localized with very low variance. However, as seen in Table 2, the small variations during training and testing make the classifiers more robust, and performance improves significantly. Initialized with a larger variance and converging to a smaller one, our data augmentation scheme can be thought of as an adaptive regularizer, smoothing the loss function more in the beginning and less towards the end of training, hereby improving optimization.



(a) Input data examples from MNIST  $\times$  KMNIST.



(b) Crops predicted by the P-STN model.

Figure 7. MNIST  $\times$  KMNIST dataset and P-STN attention.

|       | Accuracy                            | NLL                                 |
|-------|-------------------------------------|-------------------------------------|
| CNN   | $0.640 \pm 0.012$                   | $1.139 \pm 0.029$                   |
| STN   | $0.812 \pm 0.013$                   | $0.614 \pm 0.035$                   |
| P-STN | <b><math>0.894 \pm 0.003</math></b> | <b><math>0.367 \pm 0.009</math></b> |

Table 2. Performance on the MNIST  $\times$  KMNIST dataset

### 5.3. UCR time series dataset

For most data modalities, such as time series, it is not trivial to craft a useful data augmentation scheme. In this experiment, we show that the P-STN can learn a data augmentation scheme that increases performance compared to a standard CNN on the UCR time series dataset (Dau et al., 2018). The dataset is composed of 108 smaller datasets, where each dataset contains univariate time series. The FordA dataset, for example, contains measurements of engine noise over time and the goal is to classify whether or not the car is faulty. We select 7 of those subsets, each large enough to divide into training and validation set (75/25%), which we use to find the optimal  $\sigma_p$  via grid-search. The test-set is pre-defined by the dataset curators. Learning rate and optimizer are the same as in Sec. 5.1, and we perform no normalization. All models have approximately one million parameters.

Table 3 shows that the P-STN achieves higher mean accuracy than both the STN and the CNN. We note that the performance of STN and P-STN are very similar, but that both models perform better across multiple dataset than the CNN, indicating that we can automatically learn an useful data augmentation scheme for time series.

Figure 8 shows an example of the learned data augmentation. We see that the model does not simply apply the prior everywhere, but cleverly learns to augment the time series more in some intervals, such as in  $[60; 110]$ , and augment the time series less in other intervals, such as in  $[0; 50]$ .

|                   | CNN                    | STN                    | P-STN                  |
|-------------------|------------------------|------------------------|------------------------|
| FaceAll           | 0.7969 ± 0.0189        | 0.8014 ± 0.0320        | <b>0.8186</b> ± 0.0194 |
| TwoPatterns       | 0.9560 ± 0.0035        | <b>0.9977</b> ± 0.0029 | 0.9935 ± 0.0015        |
| wafer             | <b>0.9963</b> ± 0.0010 | 0.9937 ± 0.0020        | 0.9940 ± 0.0009        |
| StarLightCurvesX  | 0.9560 ± 0.0219        | 0.9478 ± 0.0406        | 0.9679 ± 0.0098        |
| uWaveGestureLib.* | 0.7456 ± 0.0104        | <b>0.7935</b> ± 0.0155 | 0.7599 ± 0.0047        |
| PhalangesOutlC.** | 0.7953 ± 0.0181        | 0.8093 ± 0.0208        | <b>0.8245</b> ± 0.0166 |
| FordA             | 0.9038 ± 0.0086        | 0.9127 ± 0.0086        | <b>0.9181</b> ± 0.0052 |
| Mean              | 0.8786                 | 0.8937                 | <b>0.8966</b>          |

Table 3. Accuracies on a subset of the UCR timeseries dataset (full dataset names are \*uWaveGestureLibrary and \*\*PhalangesOutlinesCorrect). ±1 STD is reported after 5 repetitions.

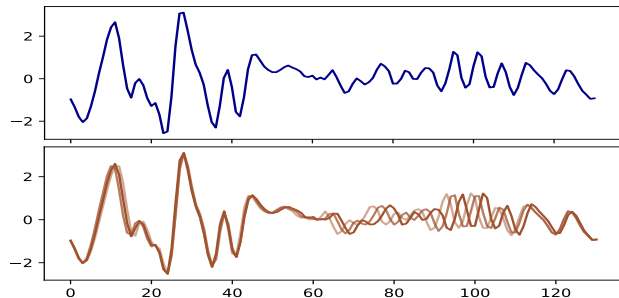


Figure 8. Examples of augmentations for a time series from the FaceAll dataset. The top plot shows the original time series and the bottom plot shows three augmented versions of the time series.

#### 5.4. CelebA

In this task, we investigate the P-STN’s performance on the challenging CelebA dataset. This dataset contains more than 200K faces of celebrities, and each face is labeled with the appearance of 40 different attributes, spanning from eyeglasses to mustaches (Fig. 10 shows a sample from the dataset). We use a similar architecture as in the MNIST × KMNIST experiment, however, in this task, we only use one branch in both the STN and P-STN, and we allow the localizer to predict the full affine transformation. Each model is trained 40 times; once for each binary attribute. In Table 4 we show that the P-STN accuracy slightly outperforms both the STN and the CNN. While DA is most valuable in the low data regime and we only see small improvements, we here demonstrate that our approach scales to large data sets as well.

|       | Accuracy        | NLL             |
|-------|-----------------|-----------------|
| CNN   | 0.878267        | 0.277425        |
| STN   | 0.893260        | <b>0.240676</b> |
| P-STN | <b>0.894331</b> | 0.240999        |

Table 4. The mean performance and standard deviation across all attributes on the CelebA dataset.

One reason for the improved performance is the learned data augmentation during training. Figure 9 shows some of

the random crops and rotations the classifier is presented for during training. These small variations increase the model’s robustness. We further see in Fig. 10 that the P-STN is able

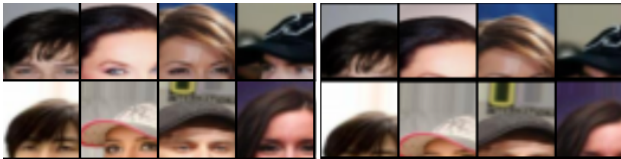


Figure 9. Shows random crops and rotations learned during training on the celebA dataset. The first column shows the input image, and the remaining columns show some of the affine transformations applied to this images.

to function as an attention mechanism. When it converges, it is able to zoom in on relevant areas of the image, e.g. for the bald attribute, the probabilistic localizers sample crops from the top of the head of the celebrities, and for the arched eyebrows attribute, the localizer focus attention around the celebrities’ eyes (Fig. 10)



(a) Shows input data from celebA.



(b) Shows the predictions of *Arched Eyebrows* (left) and *Bald* attribute (right).

Figure 10. Highlights the P-STN’s attention mechanism on the challenging CelebA dataset. Note how the localizer is able to zoom in on the relevant image regions.

## 6. Conclusion

This work introduces an end-to-end learned data augmentation scheme for neural networks, implemented as a Probabilistic extension of the Spatial Transformer network. We train the Probabilistic Spatial Transformer using variational inference. The Bayesian treatment of data augmentation allows for its application at test-time, which is experimentally shown to improve uncertainty quantification on a small subset of MNIST. Our experiments support the hypothesis that such low data regimes are where data augmentation are most crucial.

We demonstrate improved classification performance over both regular STNs and traditional DA experimentally on a variety of datasets. Besides the usual advantages of data augmentation, the P-STN introduces a varying amount of augmentation (more in the beginning, less towards the end of training). This adaptive regularization scheme improves optimization.

The improvements are especially large when we choose the family of transformations to be diffeomorphic as implemented in the CPAB library. Such complex transformations require many parameters and are practically impossible to hand-tune - our learned scheme enables us to draw on them for data augmentation. Similarly, the Probabilistic Spatial Transformer can be applied to time-series, a modality where traditional data augmentation is difficult to realize. Our Bayesian learning scheme makes the long-established practice of data augmentation applicable to new classes of transformations and modalities.

#### ACKNOWLEDGMENTS

SH and MJ are supported by a research grant (15334) from VILLUM FONDEN. This project has received funding from the European Research Council (ERC) under the European Union’s Horizon 2020 research and innovation programme (grant agreement n° 757360). We gratefully acknowledge the support of the NVIDIA Corporation with the donation of the used Titan Xp GPU.

#### References

- Baird, H. S. Document image defect models. In *SDIA*, pp. 546–556. Springer, 1992.
- Blei, D. M., Kucukelbir, A., and McAuliffe, J. D. Variational inference: A review for statisticians. *ArXiv*, abs/1601.00670, 2017.
- Blundell, C., Cornebise, J., Kavukcuoglu, K., and Wierstra, D. Weight uncertainty in neural networks. *arXiv preprint arXiv:1505.05424*, 2015.
- Dau, H. A., Keogh, E., Kamgar, K., Yeh, C.-C. M., Zhu, Y., Gharghabi, S., Ratanamahatana, C. A., Yanping, Hu, B., Begum, N., Bagnall, A., Mueen, A., Batista, G., and Hexagon-ML. The ucr time series classification archive, October 2018. [https://www.cs.ucr.edu/~eamonn/time\\_series\\_data\\_2018/](https://www.cs.ucr.edu/~eamonn/time_series_data_2018/).
- Deng, J., Dong, W., Socher, R., Li, L., Kai Li, and Li Fei-Fei. Imagenet: A large-scale hierarchical image database. In *2009 IEEE Conference on Computer Vision and Pattern Recognition*, pp. 248–255, June 2009. doi: 10.1109/CVPR.2009.5206848.
- Detlefsen, N. S. libcpab. <https://github.com/SkafteNicki/libcpab>, 2018.
- Detlefsen, N. S. and Hauberg, S. Explicit disentanglement of appearance and perspective in generative models. In *Advances in Neural Information Processing Systems (NeurIPS)*, 2019.
- Detlefsen, N. S., Freifeld, O., and Hauberg, S. Deep diffeomorphic transformer networks. In *2018 IEEE/CVF Conference on Computer Vision and Pattern Recognition*, pp. 4403–4412, June 2018.
- Engstrom, L., Tsipras, D., Schmidt, L., and Madry, A. A rotation and a translation suffice: Fooling cnns with simple transformations. *CoRR*, abs/1712.02779, 2017. URL <http://arxiv.org/abs/1712.02779>.
- Freifeld, O., Hauberg, S., Batmanghelich, K., and Fisher, J. W. Transformations based on continuous piecewise-affine velocity fields. *IEEE Transactions on Pattern Analysis and Machine Intelligence*, 2017.
- Goodfellow, I., Lee, H., Le, Q. V., Saxe, A., and Ng, A. Y. Measuring invariances in deep networks. In *NIPS*, pp. 646–654, 2009.
- Goodfellow, I. J., Pouget-Abadie, J., Mirza, M., Xu, B., Warde-Farley, D., Ozair, S., Courville, A., and Bengio, Y. Generative adversarial networks, 2014.
- Guo, C., Pleiss, G., Sun, Y., and Weinberger, K. Q. On calibration of modern neural networks. In *Proceedings of the 34th International Conference on Machine Learning - Volume 70*, pp. 1321–1330. JMLR. org, 2017.
- Hauberg, S., Freifeld, O., Larsen, A. B. L., Fisher, J. W., and Hansen, L. K. Dreaming more data: Class-dependent distributions over diffeomorphisms for learned data augmentation. In *Artificial Intelligence and Statistics*, pp. 342–350, 2016.
- Hinton, G., Vinyals, O., and Dean, J. Distilling the knowledge in a neural network. *arXiv preprint arXiv:1503.02531*, 2015.
- Hoyle, B., Rau, M. M., Bonnett, C., Seitz, S., and Weller, J. Data augmentation for machine learning redshifts applied to SDSS galaxies. *Monthly Notices of the Royal Astronomical Society*, 450:305, 2015.
- Jaderberg, M., Simonyan, K., Zisserman, A., and Kavukcuoglu, K. Spatial transformer networks. In *Advances in Neural Information Processing Systems*, pp. 2017–2025, 2015.
- Jaitly, N. and Hinton, G. E. Vocal tract length perturbation (VTLP) improves speech recognition. In *Proc. ICML Workshop on Deep Learning for Audio, Speech and Language*, 2013.
- Kanazawa, A., Jacobs, D. W., and Chandraker, M. Warpnet: Weakly supervised matching for single-view reconstruction. In *CVPR*, 2016.
- Kingma, D. P. and Welling, M. Auto-encoding variational bayes. In *2nd International Conference on Learning Representations, ICLR 2014, Banff, AB, Canada, April*

- 14-16, 2014, *Conference Track Proceedings*, 2014. URL <http://arxiv.org/abs/1312.6114>.
- Kingma, D. P. and Welling, M. An introduction to variational autoencoders. *arXiv preprint arXiv:1906.02691*, 2019.
- Krizhevsky, A., Sutskever, I., and Hinton, G. E. Imagenet classification with deep convolutional neural networks. In Pereira, F., Burges, C., Bottou, L., and Weinberger, K. (eds.), *NIPS*, pp. 1097–1105. Curran Associates, Inc., 2012a.
- Krizhevsky, A., Sutskever, I., and Hinton, G. E. Imagenet classification with deep convolutional neural networks. In Pereira, F., Burges, C. J. C., Bottou, L., and Weinberger, K. Q. (eds.), *Advances in Neural Information Processing Systems 25*, pp. 1097–1105. Curran Associates, Inc., 2012b. URL <http://papers.nips.cc/paper/4824-imagenet-classification-with-deep-convolutional-neural-networks.pdf>.
- LeCun, Y., Jackel, L., Bottou, L., Brunot, A., Cortes, C., Denker, J., Drucker, H., Guyon, I., Muller, U., Sackinger, E., et al. Comparison of learning algorithms for handwritten digit recognition. In *International conference on artificial neural networks*, volume 60, pp. 53–60. Perth, Australia, 1995.
- Lin, C. and Lucey, S. Inverse compositional spatial transformer networks. *CoRR*, abs/1612.03897, 2016. URL <http://arxiv.org/abs/1612.03897>.
- Lin, T., Maire, M., Belongie, S. J., Bourdev, L. D., Girshick, R. B., Hays, J., Perona, P., Ramanan, D., Dollár, P., and Zitnick, C. L. Microsoft COCO: common objects in context. *CoRR*, abs/1405.0312, 2014. URL <http://arxiv.org/abs/1405.0312>.
- Loosli, G., Canu, S., and Bottou, L. Training invariant support vector machines using selective sampling. *Large scale kernel machines*, pp. 301–320, 2007.
- Shapira Weber, R. A., Eyal, M., Skafté, N., Shriki, O., and Freifeld, O. Diffeomorphic temporal alignment nets. In Wallach, H., Larochelle, H., Beygelzimer, A., d’Alché-Buc, F., Fox, E., and Garnett, R. (eds.), *Advances in Neural Information Processing Systems 32*, pp. 6570–6581. Curran Associates, Inc., 2019. URL <http://papers.nips.cc/paper/8884-diffeomorphic-temporal-alignment-nets.pdf>.
- Simard, P. Y., Steinkraus, D., and Platt, J. C. Best practices for convolutional neural networks applied to visual document analysis. In *2013 12th International Conference on Document Analysis and Recognition*, volume 2, pp. 958–958. IEEE Computer Society, 2003.
- Sønderby, S. K., Sønderby, C. K., Maaløe, L., and Winther, O. Recurrent spatial transformer networks. *arXiv preprint arXiv:1509.05329*, 2015.
- Tanner, M. A. and Wong, W. H. The calculation of posterior distributions by data augmentation. *Journal of the American statistical Association*, 82(398):528–540, 1987.
- Tran, T., Pham, T., Carneiro, G., Palmer, L., and Reid, I. A bayesian data augmentation approach for learning deep models. In *Advances in Neural Information Processing Systems*, pp. 2797–2806, 2017.
- Van der Wilk, M., Bauer, M., John, S., and Hensman, J. Learning invariances using the marginal likelihood. In *Advances in Neural Information Processing Systems*, pp. 9938–9948, 2018.
- Wang, G., Li, W., Aertsen, M., Deprest, J., Ourselin, S., and Vercauteren, T. Test-time augmentation with uncertainty estimation for deep learning-based medical image segmentation. *arXiv preprint arXiv:1807.07356*, 2018.

## A. The Reconstruction Loss

In the main paper we state, that the reconstruction loss can be omitted during training, and we will elaborate on this here. Recall that the reconstruction loss is given by

$$\mathbb{E}_{q(I, \theta | I_{obs}, y)} [\log p(I_{obs} | I, \theta)], \quad (30)$$

where

$$p(I_{obs} | I, \theta) = \mathcal{N}(I_{obs} | T_{\theta}^{-1}(I), \sigma_{noise}^2 \text{Id}_d). \quad (31)$$

**Assumption A** For any  $\theta$ ,  $T_{\theta}$  is linear in its input  $x, y$

$$T_{\theta}(\alpha x + \beta y) = \alpha T_{\theta}(x) + \beta T_{\theta}(y), \quad (32)$$

where  $x, y \in \mathbb{R}^d$  and  $\alpha, \beta \in \mathbb{R}$ . Figures 11 and 12 illustrate that this is a reasonable assumption.

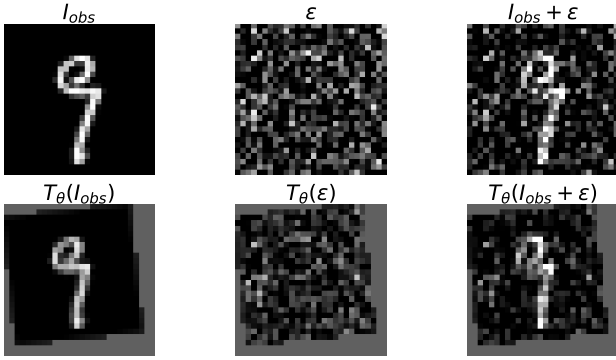


Figure 11. First row: An MNIST image, noise and sum of the two. Second row: All three transformed with  $T_{\theta}$  for a fixed  $\theta$ .

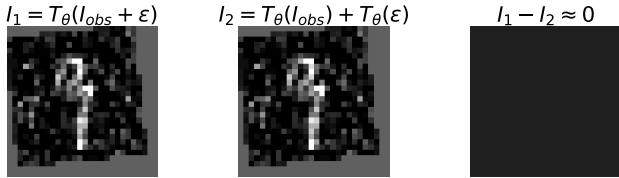


Figure 12. Transforming the summed image vs. summing the transformed images. The output is the same up to negligible quantization errors ( $\sum_{i=1}^{28 \cdot 28} I_1[i] - I_2[i] = -1.2 \cdot 10^{-5}$ , rightmost image).

Now let  $\theta$  be given. If  $T_{\theta}$  satisfies Assumption A, then trivially so does its inverse. Considering only the mean term in Eq. 31, we observe

$$T_{\theta}^{-1}(I) = T_{\theta}^{-1}(T_{\theta}(I_{obs}) + \sigma_{noise}\epsilon) \quad (33)$$

$$= I_{obs} + T_{\theta}^{-1}(\sigma_{noise}\epsilon), \quad (34)$$

where  $\epsilon \sim \mathcal{N}(0, \text{Id}_d)$ . By this observation, we can equivalently describe Eq. 31 as

$$p(I_{obs} | I, \theta) = \mathcal{N}(\sigma_{noise} T_{\theta}^{-1}(\epsilon) | 0, \sigma_{noise}^2 \text{Id}_d) \quad (35)$$

$$= \mathcal{N}(T_{\theta}^{-1}(\epsilon) | 0, \text{Id}_d) \quad (36)$$

By Assumption A, it holds that

$$T_{\theta}^{-1}(\epsilon) = T_{\theta}^{-1}(0) + \frac{\partial T_{\theta}^{-1}(0)}{\partial I} \epsilon \quad (37)$$

$$= \frac{\partial T_{\theta}^{-1}(0)}{\partial I} \epsilon, \quad (38)$$

$$(39)$$

from which we can deduct that

$$T_{\theta}^{-1}(\epsilon) \sim \mathcal{N}\left(0, \frac{\partial T_{\theta}^{-1}}{\partial I} \frac{\partial T_{\theta}^{-1}}{\partial I}^{\top}\right). \quad (40)$$

For ease of notation we now denote  $J = T_{\theta}^{-1}(\epsilon)$ , where  $J[x, y] \in [0, 1]$  is the color value at pixel position  $(x, y)$ . Denote  $[x', y'] = T(x, y)$ .

Assuming bilinear interpolation, we then have

$$J[x, y] = w_{11}\epsilon[[x'], [y']] + w_{12}\epsilon[[x'], [y']] + w_{21}\epsilon[[x'], [y']] + w_{22}\epsilon[[x'], [y']] \quad (41)$$

We will flatten the image and use vectorized notation, indexing images by  $J[i] = J[x, y]$  instead. We write  $[x], [y] =: [i]$ . Hence, we also denote  $i' = T(i)$ . Now the  $d \times d$ -matrix appearing in Eq. 40 can be denoted as  $\frac{\partial J}{\partial I}$ . We then have derivatives

$$\left(\frac{\partial J}{\partial I}\right)_{i,j} = \begin{cases} w_{11} & \text{if } j = [i'] \\ w_{12} & \text{if } j = [i'] \\ w_{21} & \text{if } j = [i'] \\ w_{22} & \text{if } j = [i'] \\ 0 & \text{else,} \end{cases} \quad (42)$$

where the  $w$ 's depend on the transformation and sum to 1 for bilinear interpolation. Thus, each column of  $\frac{\partial J}{\partial I}$  has four non-zero entries which sum to one. For translations and rotations, there is one-to-one correspondence between  $i$  and  $i'$ , i.e. each  $I[i]$  influences no more than four pixels in  $J$ , thus the rows sum to one as well, yielding a bound for the marginal distributions in Eq. 40. When we allow for scaling or stretching the grid  $\{i\}_{1, \dots, d}$ , the rows can sum to a larger value potentially blowing up the bound for the marginal covariance. However, in practice, we do not see any such degenerate transformations (see Fig. 13). This is due to the classification loss (extreme zooming into a small region of the image will usually make classification impossible) as well as the regularization towards the identity transformation via the prior  $p(\theta) = \mathcal{N}(0, \sigma_p \text{Id}_D)$ .

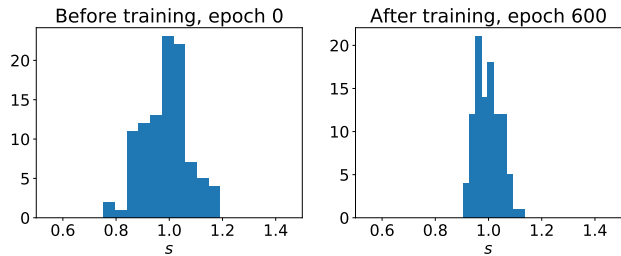


Figure 13. Histograms of the scale parameter contained in the sampled  $\theta \sim q(\theta|I_{\text{obs}})$  for all  $I_{\text{obs}}^i, i = 1, \dots, 100$  from the MNIST100 dataset. We observe no degenerate transformations.

Bounding these marginal variances are important to make the evaluations in Eq. 35 robust. In other words, degenerate scaling and stretching could have a big influence on the reconstruction loss, but other regulators already ensure that such transformation are unlikely to occur. This is visualized in Figure 13.